Elastic anomalies and long/short-range ordering effects: A first-principles investigation of the Ag_cPd_{1-c} solid solution

Martin Hoffmann,[1,2,*] Alberto Marmodoro,[2] Eero Nurmi,[3,4,5] Kalevi Kokko,[3,5] Levente Vitos,[6,7,8] Arthur Ernst,[2] and Wolfram Hergert[1]

[1]*Institute of Physics, Martin Luther University Halle-Wittenberg, Von-Seckendorff-Platz 1, 06120 Halle, Germany*
[2]*Max Planck Institute of Microstructure Physics, Weinberg 2, 06120 Halle, Germany*
[3]*Department of Physics and Astronomy, University of Turku, FIN-20014 Turku, Finland*
[4]*Graduate School of Materials Research, Turku, Finland*
[5]*Turku University Centre for Materials and Surfaces (MatSurf), Turku, Finland*
[6]*Applied Materials Physics, Department of Materials Science and Engineering, Royal Institute of Technology, Stockholm SE-10044, Sweden*
[7]*Department of Physics and Astronomy, Division of Materials Theory, Uppsala University, Box 516, SE-751210, Uppsala, Sweden*
[8]*Research Institute for Solid State Physics and Optics, P.O. Box 49, Budapest H-1525, Hungary*

(Received 13 February 2012; published 5 September 2012)

We investigate the elastic properties of the binary alloy Ag-Pd. The lattice constant of this system shows significant deviations from the linear behavior anticipated by the semi-empirical Vegard's rule. This effect was formerly studied by assuming total substitutional disorder, and described by the coherent potential approximation (CPA). Theoretical phase diagram investigations have however suggested three ordered phases at low temperatures, and we extend our first-principles investigation to include such scenarios through the adoption of an extended unit cell representation and a recently developed multisublattice generalization of the original CPA. This allows us to explore equilibrium lattice constant and bulk modulus within a unified approach even in the presence of partial long-range order. We obtain significant variations of the bulk modulus in comparison to the totally disordered picture, and again very rich deviations from more intuitive predictions of a simple linear behavior. We follow former suggestions to analyze the different regimes in connection with topological transitions of the Fermi surface, examined through Bloch spectral function calculations.

DOI: 10.1103/PhysRevB.86.094106 PACS number(s): 61.43.−j, 62.20.−x, 64.70.kd, 64.60.Cn

I. INTRODUCTION

The equilibrium lattice constant of substitutional solid solutions follows to the leading order an approximate relationship, suggested by Vegard,[1] that predicts a linear change of volume while changing the concentration of the constituents. However, strict adherence to Vegard's law is more an exception than the rule in real materials.

Moreover, solid solutions at certain concentrations may form fully ordered phases. As an example, the well known Cu-Au system gives rise to $L1_2$ and $L1_0$ crystals, respectively, at $c_{Au} = 0.25$ and 0.50. In these regimes, the materials have different electrical, magnetic and mechanical properties compared to their fully disordered counterparts. Hence, a detailed theoretical investigation of the deviations from Vegard's rule is important in order to gain deeper insight in the structural and electronic properties of compounds over the whole phase diagram.

We will focus our investigation on the Ag_cPd_{1-c} alloy system, which forms solid solutions over the entire concentration range $c \in [0,1]$. Bruno *et al.*[2–4] have previously examined such system from the point of view of variations in the Fermi surface as a function of the constituents' ratio, in a fixed face centred cubic (fcc) reference geometry. Substitution of Pd with Ag changes the topology of the Fermi surface drastically, and so-called Lifshitz or electronic topological transitions (ETT) occur. Bruno *et al.* remarked how such concentration-dependent transitions should influence the equilibrium properties. More recently, Delczeg-Czirjak *et al.*[5] have calculated the equilibrium properties of Ag-Pd, including the bulk modulus and the single-crystal elastic constants, over the whole concentration range for the same fully disordered picture. They observed an anomalous nonlinear behavior in such quantities, and connected this successfully with the ETT's highlighted by Bruno *et al.* The above calculations are however based on the coherent potential approximation (CPA), a theory well known not to include short-range order (SRO) effects beyond single-site substitutions.

Müller and Zunger performed an unbiased theoretical search for long-range ordered (LRO) structures in the same Ag-Pd system.[6] They predicted three ordered structures at $c = 0.25$, 0.5, 0.75: $Ag_{0.75}Pd_{0.25}$ in an ordered $L1_2$ phase (Cu_3Au prototype), $Ag_{0.5}Pd_{0.5}$ in a $L1_1$ phase (CuPt prototype) for $c = 0.50$, and "$L1_1^+$" at $Ag_{0.25}Pd_{0.75}$ (similar to the $L1_1$ geometry but with different on-site occupancy). Later, Ruban *et al.*[7] found a long-period superstructure (LPS) as marginally more stable for $Ag_{0.75}Pd_{0.25}$. Such a LPS exhibits periodic antiphase boundaries. For $c = 0.75$, the distance between the boundaries is $3 \times a$ that introduces a new periodicity of $2(3 \times a)$ in the lattice (abbreviated with LPS3). Not all these structures have been to this date experimentally observed.

The main goal of our investigation is the study of the influence of SRO and LRO on the equilibrium properties of the Ag_cPd_{1-c} alloy system. We examine it by adopting the Korringa-Kohn-Rostoker (KKR) method, and also compare results with exact muffin-tin orbital (EMTO) calculations.[5] Both techniques are based on multiple scattering theory and are particularly well suited for the study of disordered systems, modeled with the coherent potential approximation (CPA) and its further developments.

SRO effects have been examined by taking advantage in particular of the nonlocal extension to the originally single-site

theory, in its simple[8] (NL-CPA) and multisublattices per unit cell[9,10] (MS-NL-CPA) generalizations. We also consider LRO structures by adopting an *ad hoc* supercell, twice as large as the conventional setup for an fcc lattice. Variations of concentration on certain sites in this larger unit cell allow to approach the different LRO structures, and investigate the whole concentration range. We compute in particular macroscopic equilibrium properties such as the equilibrium volume and bulk modulus, and microscopic ones such as the Bloch spectral function (BSF) $A_B(\boldsymbol{k},\epsilon)$. The Fermi surface topology thus revealed is then examined in its connection with elastic anomalies over this more accurate scenario.

The paper is organized as follows. Section II provides the details of the computational techniques. At first, a short overview on the Korringa, Kohn, and Rostoker (KKR) and exact muffin-tin orbitals (EMTO) methods is given. Subsequently, we discuss the basic aspects of how calculations of elastic properties were performed. At the end of the section, we also introduce the details of the supercell approach for the inclusion of SRO and LRO effects.

Results obtained in the framework of a single-site theory are given in Sec. III. Our calculations are compared with former theoretical findings[5] and experimental work.[11,12] An interpretation is offered in the context of Vegard's law[1] for metallic alloys, and the basic insights provided by a more general, semiqualitative free electrons gas model.[13] In Sec. IV, effects beyond single-site substitutions are discussed. At first, the outcome of supercell calculations of long-range order is examined (see Sec. IV A). Some short-range order regimes are then also included (see Sec. IV B), again in connection with the changes observed in the associated Fermi surface. Overall conclusions are drawn in Sec. V.

II. THEORETICAL METHODS

A. Basics of KKR and EMTO method

Our implementation of the general KKR method[14] provides a variety of tools for the description of partially or totally disordered systems. The main quantity of interest for the first-principles determination of elastic properties is the total energy as a function of lattice strain. The required accuracy can also be achieved in the EMTO method,[15–18] which shares a similar approach to the solution of the electronic problem in a solid.

In the KKR-GF method, the material is modelled as a collection of ions arranged in a regular lattice, interacting with the electrons through individual atomic potentials only up to a certain cutoff distance. Such effective single-particle potentials are, in particular, determined within density functional theory, through the search for an appropriate non-interacting solution to the Kohn-Sham equations. In this study, we resort to the full-charge density approximation[19] (FCDA), which has proved to give comparable results with lower numerical effort than the full-potential approaches.

These potentials control the scattering of an incoming electronic wave, which has to be identical to the superposition of all other outgoing waves. The process is described by the scattering path operator $\underline{\tau}^{ij}(\epsilon)$:

$$\underline{\tau}^{ij}(\epsilon) = \{[\underline{t}(\epsilon)^{-1} - \underline{G}^0(\epsilon)]^{-1}\}_{ij}, \tag{1}$$

for indices i,j labeling arbitrary portions of the sample. In this formulation, "chemical" aspects of the single-particle potentials, expressed within the t matrix term, and the geometrical properties of the underlying lattice, given in the structure constants $\underline{G}(\epsilon)$, are decoupled. This makes such technique particularly well suited for the study of substitutional disorder problems. All observables can then be obtained from the Green's function $\mathcal{G}(\boldsymbol{k},\epsilon)$.

In this approach, the CPA is widely used to model the locally unknown distribution of different atomic species on the lattice through an effective medium description[20] in which the same self-consistently determined t matrix appears on every scattering site and on-average translational invariance is restored. This description allows to evaluate Eq. (1) as

$$\bar{\underline{\tau}}^{ij}(\epsilon) = \frac{1}{\Omega_{BZ}} \int_{\Omega_{BZ}} d\boldsymbol{k} [\bar{\underline{t}}^{-1}(\epsilon) - \underline{G}^0(\mathbf{k},\epsilon)]^{-1} e^{+i\mathbf{k}\cdot(\mathbf{R}_i - \mathbf{R}_j)}. \tag{2}$$

Such quantity is determined self-consistently at each energy ϵ. The average t-matrix approximation (ATA) $\bar{\underline{t}}_{\text{init}} = c_{\text{Ag}}\underline{t}_{\text{Ag}} + c_{\text{Pd}}\underline{t}_{\text{Pd}}$ provides an initial ansatz, which is complemented with the requirement that, on average, no extra scattering should take place on any site. Upon convergence, all average properties can be studied straightforwardly, and without the artefacts' deriving from spurious periodicity in boundary conditions or atomic potentials' distribution.

This general strategy is also followed in the EMTO method. Among the main differences may be identified a different way of partitioning the lattice space, which is decomposed into a collection of large, overlapping spheres around each atom. A central scattering potential is considered inside each of these domains, and assumed constant in the remaining interstitial regions. Such construction is then optimised to give the best possible spherical approximation to the exact potential, minimising deviations between the exact and overlapping potentials, and the errors due to the intersection of different spheres.[15,18]

With respect to the DFT part of the above multiple scattering treatments, systematic EMTO studies have already investigated the influence of different exchange-correlation functionals choices for this class of applications.[5] While the equilibrium lattice constant would best reproduce experimental values[11] by using the PBEsol exchange-correlation functional,[21] the evaluation of elastic anomalies as defined below [see Eq. (4)] appears to be possible also within the local-density approximation (LDA). Cancellation of systematic underestimation effects takes in fact place when evaluating deviations from equilibrium properties. These findings are summarised in Fig. 2, comparing experimental results with those from different exchange-correlation functional choices within the EMTO (LDA, PBEsol), and KKR (LDA) methods. Therefore the LDA form of Perdew and Wang[22] has been used in this work.

B. Calculation of elastic properties

Equilibrium lattice parameter and bulk modulus can be obtained by fitting the results of total energy calculations for a series of different unit cell volumes V to the

Birch-Murnaghan[23,24] equation of state:

$$E(V) = E_0 + \frac{9}{16} B_0 V_0 \left\{ \left[\left(\frac{V_0}{V} \right)^{2/3} - 1 \right]^3 B_0' - \left[\left(\frac{V_0}{V} \right)^{2/3} - 1 \right]^2 \left[4 \left(\frac{V_0}{V} \right)^{2/3} - 6 \right] \right\}. \quad (3)$$

Four independent parameters are thereby estimated: the equilibrium total energy E_0, the equilibrium volume V_0, the bulk modulus B_0, and the pressure derivative of the bulk modulus B_0', normally used for the calculation of the Grüneisen constant.

For our study of Ag_cPd_{1-c}, this procedure has been applied to an evaluation of 17 different atomic volumes, chosen around the average value of $\bar{a}^{fcc} = 7.43$ a.u. between the Ag and Pd equilibrium lattice constants ($a_0^{Pd} = 7.2794$ a.u. and $a_0^{Ag} = 7.5930$ a.u.). We repeat the calculations at $\pm 0.5\%$ lattice constant intervals over the whole concentration range $c \in [0,1]$. This choice ensures that for the fitting procedure a sufficient number of volumes is located left (right) of the theoretical equilibrium volume. The use of alternative equations of state, such as Morse[25] or Murnaghan ones,[26,27] only leads to minor variations in the results of interest for this case study.

Difference in smoothness of this total energy versus the concentration landscape may be ascribed to the typical softening of effective medium features for $c \neq 0$, 1, to be contrasted with the sharper band structures of the pure elements. In the pure systems, the variation of volume can lead to more likely discontinuities in the occupation of states near the Fermi surface, including a sudden variation on the total energy that affects the convergence of numerical fits like Eq. (3).

Anomalies in the properties of a general equilibrium property A are defined by considering the difference between linear estimates extrapolated from the values of c alone, and the actual outcome of calculations at that concentration:[5]

$$\Delta A(c) = A(c) - A^{lin}(c), \qquad A^{lin}(c) = A(0) + c[A(1) - A(0)], \quad (4)$$

where $A(0)$ and $A(1)$ are the corresponding values for pure Pd and Ag, respectively.

C. Extended setup for LRO/SRO

To investigate LRO and SRO effects, the reference structures have to be set up. For the single-site CPA description of Ag_cPd_{1-c} due to the effective medium formulation, only a simple face centred cubic (fcc) lattice is necessary. Müller and Zunger[6] pointed out, however, that three long-range ordered structures ($L1_1^+$, $L1_1$, $L1_2$) should exist in the AgPd alloy system. Those three structures differ in assigning specific elements to particular sites in a large enough supercell, constructed from an underlying fcc lattice. The LPS3 structure found by Ruban *et al.*[7] would dramatically increase the size of the supercell placing it for now beyond the numerical abilities of the MS-NL-CPA. Therefore we restricted our study to the $L1_2$ structure.

The corresponding extended setup (ES) is then given by the basis $\mathbf{R}_1^{ES} = a^{ES}(1.,0.,0.)$, $\mathbf{R}_2^{ES} = a^{ES}(0.5,0.5,0.)$, $\mathbf{R}_3^{ES} = a^{ES}(0,0.5,0.5)$, with rescaled lattice constant $a^{ES} = 2a^{fcc}$, and the sublattice positions reported in Table I. Figure 1 depicts schematically such supercell. In this framework, a transition from one ordered structure to another one corresponds to a variation in concentration from $c_s = 0 \rightarrow 1$ on specific sublattices s.

TABLE I. List of the $N_{sub} = 8$ nonequivalent sublattices used to compare the three LRO structures $L1_1$, $L1_2$ and $L1_1^+$ within a unified framework, in the supercell with basis vectors: $\mathbf{R}_1^{ES} = a^{ES}(1.,0.,0.)$, $\mathbf{R}_2^{ES} = a^{ES}(0.5,0.5,0.)$, $\mathbf{R}_3^{ES} = a^{ES}(0,0.5,0.5)$ (see text).

Sublattice	Origin	Sublattice	Origin
$\mathbf{a}_1$	(0.00,0.50,0.00)	$\mathbf{a}_5$	(0.00,0.00,0.00)
$\mathbf{a}_2$	(0.25,0.25,0.00)	$\mathbf{a}_6$	(0.25,0.75,0.00)
$\mathbf{a}_3$	(0.00,0.25,0.25)	$\mathbf{a}_7$	(0.00,0.75,0.25)
$\mathbf{a}_4$	(0.25,0.50,0.25)	$\mathbf{a}_8$	(0.25,1.00,0.25)

If a specific alloy characterised by the Ag concentration c is considered, the total concentration is related to the sublattice concentrations by $c = \frac{1}{N_{sub}} \sum_{s=1}^{N_{sub}} c_s^{Ag}$. Different occupations of the sublattices lead to the same global Ag:Pd ratio. This offers a high degree of flexibility to examine very different structures within a unified setup.

Figure 1 illustrates two particular situations. The transition between the $L1_1^+$ and $L1_1$ structures ($c = 0.25$, 0.5) is depicted on the left hand side. The sublattices $\mathbf{a}_i$, $i = 1, \ldots, 6$ are fixed and occupied by an Ag, four Pd and again an Ag atom, respectively; whereas the two sublattices sites $\mathbf{a}_7$ and $\mathbf{a}_8$ exhibit the same concentration $c_7 = c_8$ with $c_7 \in [0,1]$ varying from pure Pd ($c_7 = 0$) to pure Ag ($c_7 = 1$).

The same procedure can be applied for a transition between the $L1_1$ and $L1_2$ structures ($c = 0.5$, 0.75), where this concentration range is limited to $c_1 = 1$, 0, while the Ag concentration on the remaining sublattices varies like $c_1 \in [1,0]$, $c_2 = c_3 = c_4 = 1 - c_1$. The sublattices $\mathbf{a}_5$, $\mathbf{a}_6$, $\mathbf{a}_7$, and $\mathbf{a}_8$ are instead occupied by Pd, Ag, Ag, and Ag, respectively.

III. SINGLE-SITE THEORY

We start our discussion in the framework of the single-site CPA theory. The total energy associated with varying unit cell volume V in Eq. (3) has been evaluated by KKR calculations, performed with full Brillouin zone sampling over a Monkhorst-Pack $80 \times 80 \times 80$ **k**-points mesh ($\approx$11 000 evaluations over the irreducible wedge). The spherical harmonics expansion cutoff value was set to $l_{max} = 4$, using the full charge density approximation to also account for nonradial charge distribution.

Results for the equilibrium lattice constant are given in Fig. 2. We compare the CPA data with a previous EMTO study,[5] in which the impact of different exchange-correlation functional choices has been investigated and compared with experiment. In particular, we note good reproduction of the main features such as the maximum deviation from linearity, absolute values of these deviations $\Delta a_0(c)$, and slope of the curves.

Substantial agreement was observed when using either the local density (LDA) or generalized gradient (GGA) approximations, both similarly capable of following the actual

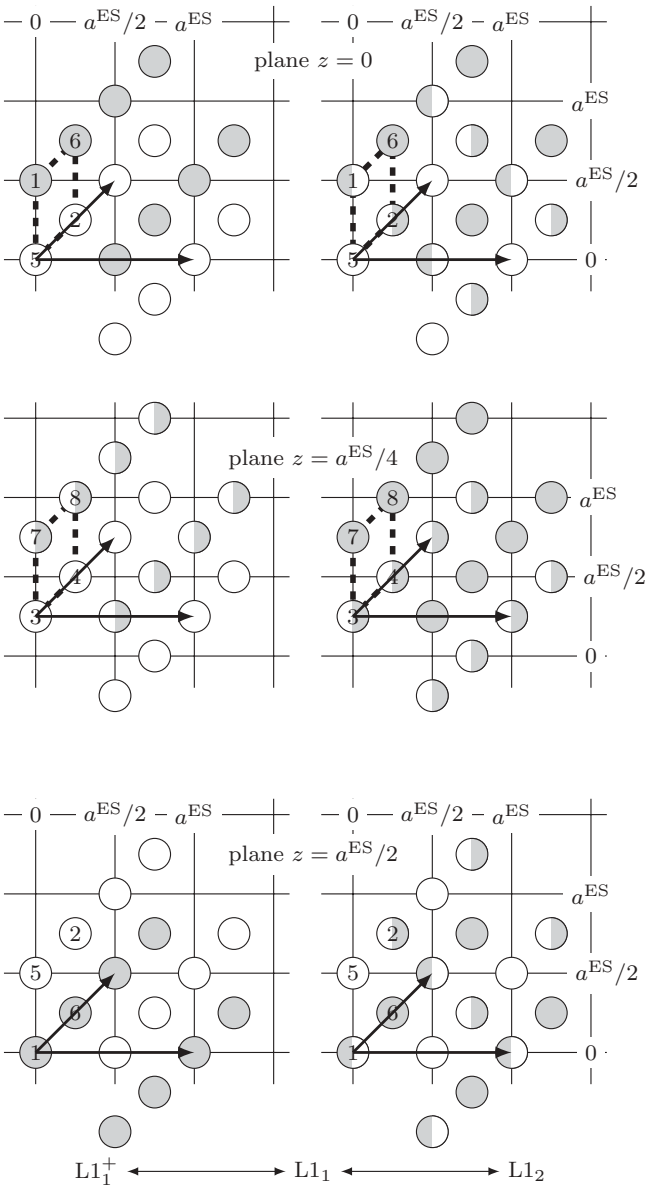

FIG. 1. Schematic representation of the extended setup adopted in Sec. IV. Circles with different fill at the nodes of a fcc lattice (underlying grid) denote different atomic species: ● for Ag, ○ for Pd, ◑ for a site at noninteger occupancy, changing from Pd to Ag with higher concentration c; and ◐ for a site at noninteger occupancy, changing from Ag to Pd. The left-hand side depicts the transition between the $L1_1^+$ and $L1_1$ ordered structures, and the right-hand side is the similar transition between $L1_1$ and $L1_2$ ones. This is illustrated for better clarity along three slices orthogonal to the z axis, at $z = 0, 0.25$, and 0.5. The coordinate system follows the edges of the single-site fcc cell. The thick dashed lines link the basis sites in the corresponding plain. The arrows denote the lattice vectors with the third vector in (0,0.5,0.5) direction. Furthermore, by treating the remaining Ag or Pd atoms for $L1_1^+$ or $L1_2$, respectively, with CPA the transition to either of the pure phases can be explored.

experimental trend. This conclusion motivates our choice of LDA in our further KKR investigations.

To the first approximation, the essential physics of equilibrium lattice parameter deviations from linearity may already be understood in a semiqualitative nearly free electrons model (see Fig. 3).[13,28] Coming then to the bulk modulus, after removal of the linear component obtained from B_0 calculations for pure Ag and Pd phases we again observe good agreement between the KKR and EMTO methods (see also Table II). In particular, different choices of exchange-correlation functionals mostly affect the mismatch of the absolute value in comparison to the predicted[29] and observed[11] bulk modulus, but such effect is removed in the present differential analysis.

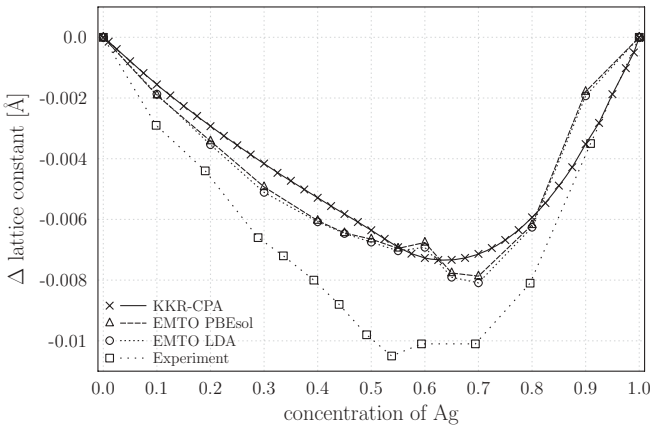

FIG. 2. Nonlinear component of the equilibrium lattice constant from single-site LDA KKR-CPA calculations (see text), compared with EMTO-CPA[5] evaluations of different exchange-correlation functionals. Experimental values[11] are also depicted.

Further understanding of such an elastic anomaly curve $\Delta B_0(c)$ requires a more accurate examination of the detailed electronic structure of the system. We follow Delczeg-Czirjak *et al.*[5] in focusing our attention on the changes in the Fermi surface topology, as obtained from Bloch spectral function calculations.[3,4] As originally showed by Bruno *et al.*, a continuous change in concentration can lead to a series of discrete transitions: for certain ratios of the Ag, Pd constituents, the connectivity of the Fermi surface may change radically, as

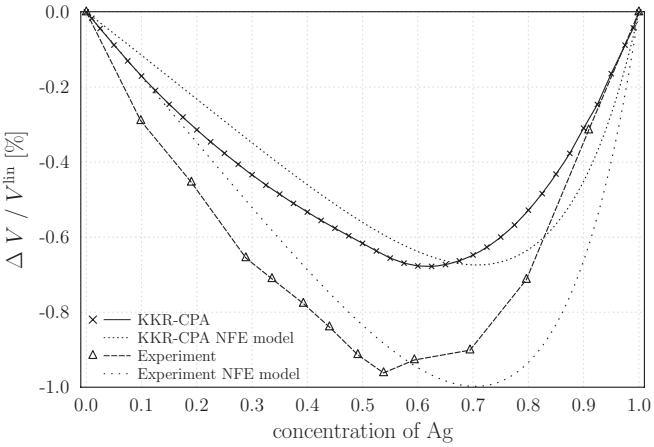

FIG. 3. Ratio of the nonlinear component of the equilibrium volume over linearly fitted estimate V^{lin}, in percent. Results from the single-site calculation (solid line, crosses) are compared with experimental values[11] (dashed line, triangles). Two dotted lines also depict predictions from a simplified nearly-free-electron approach.[13]

TABLE II. Bulk modulus B_0 for the pure constituents Pd and Ag, evaluated through different methods. A numerical uncertainty for first principles KKR and EMTO results can be estimated from the fit of the numerical data to the Birch-Murnaghan equation of states in Eq. (3). Experimental values[12] are derived from single-crystal elastic constants c_{11} and c_{12} as $B_0 = (c_{11} + c_{12})/3$.

	B_0 (GPa)	
Method	Pd	Ag
Ref. 29	180.0	110.0
EMTO LDA	222.26 ± 0.22	135.708 ± 0.077
KKR LDA	217.06 ± 0.23	131.003 ± 0.086
Experiment	187.66	102.00

some necks close or new ones develop between repeated instances of the Brillouin zone. Such variations have been linked with changes in the trends of the elastic properties as a function of concentration, which represent the main focus of our study.

In order to facilitate the understanding of this connection, we depict elastic anomalies plots of the bulk modulus $\Delta B_0(c)$ underneath a color-coded representation of the Bloch spectral function for the alloy $A_B(\mathbf{k},\epsilon) = -\frac{1}{\pi}\Im\overline{\mathcal{G}}(\mathbf{k},\epsilon)$, evaluated at the Fermi energy $\epsilon = E_F$ for each concentration c (see Figs. 4, 7, and 8). The particular path followed within the first Brillouin zone is also shown.

In this representation, vertical red lines mark particular concentration values where microscopic changes in the Fermi surface appear associated with slope variations in the corresponding estimate for macroscopic bulk modulus deviations from linearity. The relative smoothness of single-site CPA effective medium results leaves, however, some uncertainty with respect to the exact placement of such boundaries. A systematic comparison suggests here as significant the concentration intervals $c \in [0, \simeq 0.35]$, $c \in [\simeq 0.35, \simeq 0.5]$, $c \in [\simeq 0.5, \simeq 0.625]$, $c \in [\simeq 0.625, \simeq 0.725]$, and $c \in [\simeq 0.725, 1]$. Further differential analysis of the $\Delta B_0(c)$ curve slope also supports this splitting; in particular, two kinds of qualitatively different features in the BSF can be highlighted. The merging of a bifurcation (such as at $c \simeq 0.4$ when coming from the Ag-poor regime, or at $c \simeq 0.675$ when coming from the Ag-rich one) seems to be connected with a discontinuity in $\frac{d}{dc}\Delta B_0(c)$. Disappearance of bands (such as in the $c \in [0.5,625]$ interval) can, instead, be associated with changes to a negative slope in $\Delta B_0(c)$.

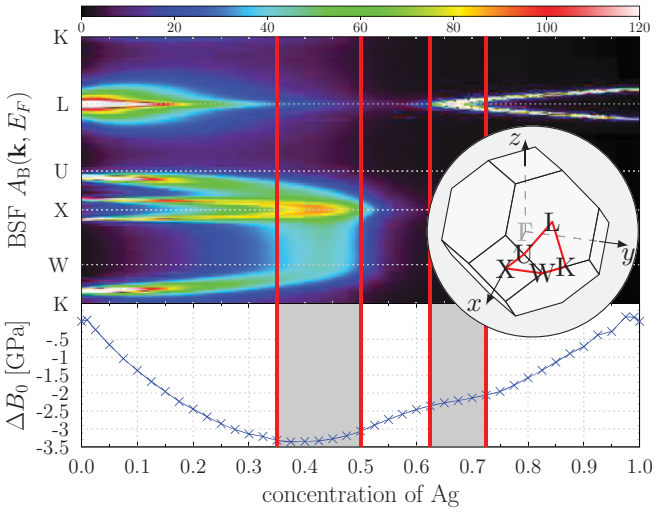

FIG. 4. (Color) Bloch spectral function (in arbitrary units) along the **K**-**W**-**X**-**U**-**L**-**K** reciprocal space path (inset, in red) evaluated at the Fermi energy, for different concentrations c in a single-site CPA study of the Ag_cPd_{1-c} system. Values in between the $c = 0.025$ intervals (blue crosses) are linearly interpolated and we relate our discussion only to these concentrations. Red vertical lines mark substantial changes in the Fermi surface topology, which may be correlated to variations of the bulk modulus deviations depicted underneath. Different connected regimes are emphasised by changing shades of white and grey.

Comparing our results over the whole concentration range with Bruno's *et al.* report,[4] suggesting five ETT's at $c = 0.06$, 0.20, 0.35, 0.53, and 0.70, our adoption of a semi-relativistic KKR treatment appears capable of resolving only two transitions. This variation can be understood with consideration of the band structure of pure Pd. In a semirelativistic calculation, two bands around the **X** point are left degenerate,[4] which is why they contribute only to a single ETT around $c \simeq 0.4$ (see Fig. 4). The relativistic features in the Pd-rich regime at $c = 0.06$, 0.20 also arise from minor changes at the boundary of the Brillouin zone, now around the **L** point. For the Ag-rich regime instead, a single ETT at $c = 0.70$ persists unchanged in both cases, due to the similar Fermi surface of pure Ag when evaluated in semi- or fully relativistic treatments.

Due to varying the concentration of the components in the alloy, we observe with the semirelativistic calculations a direct relation between the equilibrium property variations and changes in the connectivity of the Fermi surface. This statement holds also for the fully relativistic treatment.[4] Such a study may result in a similar Fig. 4, with the BSF showing sharper and more resolved peaks at low Ag concentration around the **L** point and in the region of $c \in [0.3,0.5]$. However, for a qualitative study of the relation between ΔB_0 and the $A_B(\mathbf{k}, E_F)$, the semirelativistic framework appears sufficient and well comparable with former EMTO results.[5]

IV. BEYOND SINGLE-SITE EFFECTS

Using the extended setup treatment described in Sec. II C, we continue our study of elastic anomalies to also include some recently predicted LRO cases[6] and the nearby regions of the compound phase diagram. In this approach, the material is now characterised by a set of $N_{\text{sub}} = 8$ concentrations, one for each sublattice of an extended fcc supercell representation (see Fig. 1). The fully uncorrelated alloy may still be obtained by assigning the same concentration to each site, regardless of its coordination with neighbours. Comparable results with respect to single-site calculations only require then to account for the enlarged direct space volume, through a sparser sampling for the reciprocal space Brillouin zone integrals [only $80^3(a^{\text{fcc}}/a^{\text{ES}})^3 \simeq 64\,000 = 40^3$ **k** points are used for the whole supercell Ω^{ES}].

We are, however, now in a position to evaluate in better detail two additional regimes: the case of random deviations from a set of reference long-range order $L1_1^+$, $L1_1$, and $L1_2$ structures (see Sec. IV A), and the effect of particular sorts of

short-range ordering variations within this general picture (see Sec. IV B).

A. Long-range order

The extended setup of Fig. 1 includes the three above LRO structures as a particular case of integer occupation by either Ag or Pd on each site of the complex unit cell. The higher stability of these crystalline phases with respect to the fully uncorrelated CPA results can be appreciated with consideration again to the equilibrium total energy deviation from linear behavior. Over the whole concentration range, the extended setup exhibits a lower total energy when on-site occupancy is varied only on those sublattices which are not fixed to a reference constituent, shared by at least two LRO structures (see Fig. 5).

At the Ag:Pd ratios 1 : 4, 1 : 1, and 3 : 4, we obtain as expected three clear local minima, corresponding to the $L1_1^+$, $L1_1$, and $L1_2$ geometries. This is better illustrated in the plot insets. On the left-hand side, the deviation from linear behavior of total energy when going between the pure Pd and the $L1_1$ structures (sites $\mathbf{a}_5$–$\mathbf{a}_8$ fixed) highlights a local minimum for the newly suggested[6] $L1_1^+$ ordered phase.

On the right-hand side, only a smaller range of concentrations is depicted, with $c \in [0.75,1]$. This interval is chosen to emphasise the appearance of a concave deviation from linearity, which hints to another possible ordered phase in this concentration range of the Ag_cPd_{1-c} alloy. The LPS3 structure[7] was found to be about 6 meV/atom more stable than the $L1_2$ structure, representing about 10% of the calculated formation energy for the $L1_2$ phase. Thus, taking into account the formation energy for the LPS3 in Fig. 5 does not rule out

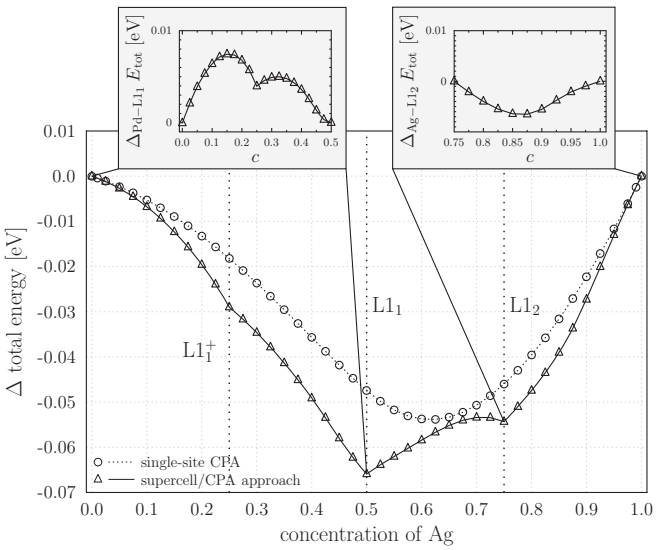

FIG. 5. Nonlinear component of the equilibrium total energy vs total concentration, for the single-site representation of the compound (circles) and the supercell described in Fig. 1/Table I (triangles). A global minimum in the trend of total energy is found for $c = 0.5$, upon realisation of the $L1_1$ LRO structure. Local minima also appear at $c = 0.75$ for the $L1_2$, and $c = 0.25$ for the $L1_1^+$ structures. Insets repeat such differential analysis over the $c \in [0,0.5]$ and $c \in [0.75,1.]$ intervals. Negative curvature seems to hint towards the existence of an additional ordered structure, located between $c = 0.85$ and 0.9.

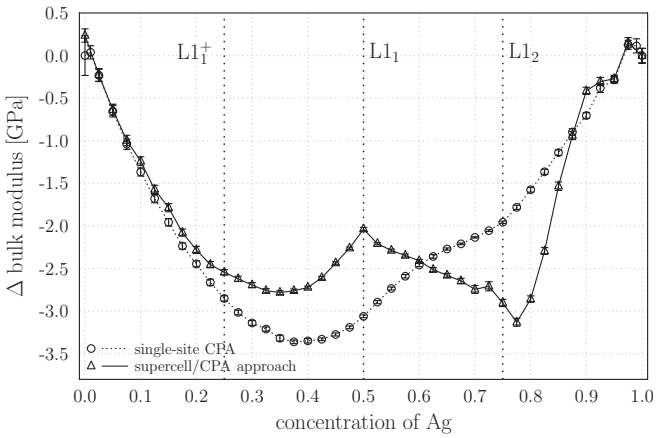

FIG. 6. The nonlinear component of the bulk modulus vs total concentration c, for a single-site representation of the compound ($N_{sub} = 1$, circles, same as the lower panel of Fig. 4), and the extended setup described in Table I ($N_{sub} = 8$, triangles). Error bars estimates from the equation of states fitting procedure are also given.

the existence of another ordered phase in the $c \in [0.75,1.]$ interval. A first structure investigation found only unstable structures and a complete search is beyond the main topic of this work. Therefore we refer at this point to a future work.

Substitutions that leave occupancy on sites $\mathbf{a}_1, \ldots, \mathbf{a}_6$ (interval $c \in [0.25,0.5]$, between $L1_1^+$ and $L1_1$ structures) or $\mathbf{a}_5, \ldots, \mathbf{a}_8$ (interval $c \in [0.5,0.75]$, between $L1_1$ and $L1_2$) fixed represent a particular case of LRO. In this portion of our study, we assume the same concentration of Ag on all remaining disordered sublattices ($c_7 = c_8$ for $L1_1^+ \longleftrightarrow L1_1$, $c_2 = c_3 = c_4 = 1 - c_1$ for $L1_1 \longleftrightarrow L1_2$), and proceed to determine bulk modulus deviations from linearity using the same procedure as outlined in Sec. III. A comparison of these results with single-site CPA evaluations shows significant differences in elastic anomalies and BSF over the whole concentration range (see Fig. 6). The variation of bulk modulus in absolute terms lies in the range of 1–1.5 GPa, and reflects similar findings in the order versus disorder differences obtained in a recent, independent EMTO study of the $Ag_{0.5}Pd_{0.5}$ case.[30]

When considering deviations from linear dependency as depicted in the figure, most concentrations in the $L1_1^+ \longrightarrow L1_1$ regime ($c \in [0.25,0.6]$) show more significant elastic anomalies than in the single-site CPA study. At $c \approx 0.6$, however, a qualitative change takes place. This trend reversal may result from structural differences between the $L1_1^+$ and $L1_1$ versus $L1_2$ arrangements of the unit cell. The latter case represents an isotropic construction, while both the former ones describe an anisotropic structure along the [111] direction (see Fig. 1, left). In particular, for the $L1_1$ case, Delczeg-Czirjak *et al.*[30] showed that the structural anisotropy translates into different compressibilities along the a and c axis. The ordered $L1_1$ phase consists in fact of alternate Ag and Pd layers, perpendicular to the c axis, and has a larger bulk modulus that places related arrangements also closer to the ideal, linear $B_0(c)$ trend of Vegard's law.

This can be contrasted with the totally disordered case, with fully random distribution of Ag and Pd atoms. More significant elastic anomalies may be understood by considering the underlying assumptions leading to the above rule. The expectation

of a linear behavior finds its origin in the idea of simple combination of bulk moduli of the two pure elements, only weighted by the relative concentration. A layered arrangement such as the $L1_1$ structure describes the regular repetition of the same elements along parallel planes. This sort of phase separation may reasonably lead to expect higher robustness of individual pure elements' properties against the stronger smearing of a fully disordered distribution. This hypothesis may be tested by considering other cases of even larger alike elements repetition. Increasing the layer thickness of the reference $L1_1$ structure from an Ag/Pd/Ag/Pd/Ag/Pd stacking (corresponding to $ABC\ ABC$ in the [111] direction of the fcc cell) to the AgAg/PdPd/AgAg/. . . sequence (with $ABC\ ABC\ ABC\ ABC$), we observe indeed further reduction of bulk modulus deviations from linearity by ≈1 GPa, despite loss of stability for such rather artificial arrangement.

Similar arguments may be applicable for the $L1_1^+$ reference. In this case, structural anisotropy is reduced because of the development of Ag chains perpendicular to the [111], [$\bar{1}$10] and [001] directions (see Fig. 1, left). This does not apply instead to the more isotropic $L1_2$ structure, which cannot be simply modified to form layers or chains in any particular directions. The stiffer constituent Pd always forms only a loose "skeleton" of atoms, embedded within an Ag matrix.

We now revert our analysis to the investigation of the possible microscopic origin of elastic anomalies, focusing in particular on variations in the topology of the Fermi surface now examined under the above assumption of partial LRO. In comparison with the single-site BSF calculation (see Fig. 4), an integer occupancy on some sublattices gives rise to a generally sharper band structure over the whole concentration range (see Fig. 7).

Two different regimes may be noted. For $c \in [0,0.5]$, the d bands of Pd cross the Fermi level and are depicted as a rich set of clearly resolved features along all reciprocal space paths, as the amount of Ag increases. This may be contrasted with the simpler outlook of a similar first part of the plot for the CPA results of Fig. 4: most features appear there smeared out and are left unresolved in the fully uncorrelated, single-site approach.

Actual concentrations where such topology changes occur are however different, and dependent on the particular direction taken into consideration. When it comes to evaluating an integrated-over quantity such as the bulk modulus deviations $\Delta B_0^{\mathrm{ES}}(c)$, the impact of different features' changes is combined. A differential analysis of the elastic anomalies slope leads then to identify three main transitions in the first half of Fig. 7, for $c \simeq 0.225$, $c \simeq 0.325$, and $c \simeq 0.425$. More specifically, the first feature may be associated with the merging at $\mathbf{X}_1$, while the subsequent interval $c \in [0.325,0.425]$ could be correlated with changes occurring at $\mathbf{L}_1$. Further points towards $c = 0.5$ relate to completing the merge at $\mathbf{K}_2$ or $\mathbf{U}_2$. However, the dominant closure of two peaks at $\mathbf{L}_2$ does not seem observable in ΔB_0^{ES}, which may be related to an unique character of this feature which is linked to a threefold symmetry axis due to the layered stacking in the region $c \in [0.5,0.75]$.

When the content of silver exceeds $c = 0.5$, only the sp bands cross the Fermi level. This leads to a simpler outcome, again comparable to the same concentration interval in Fig. 4. In this regime, different topological transitions do not overlap

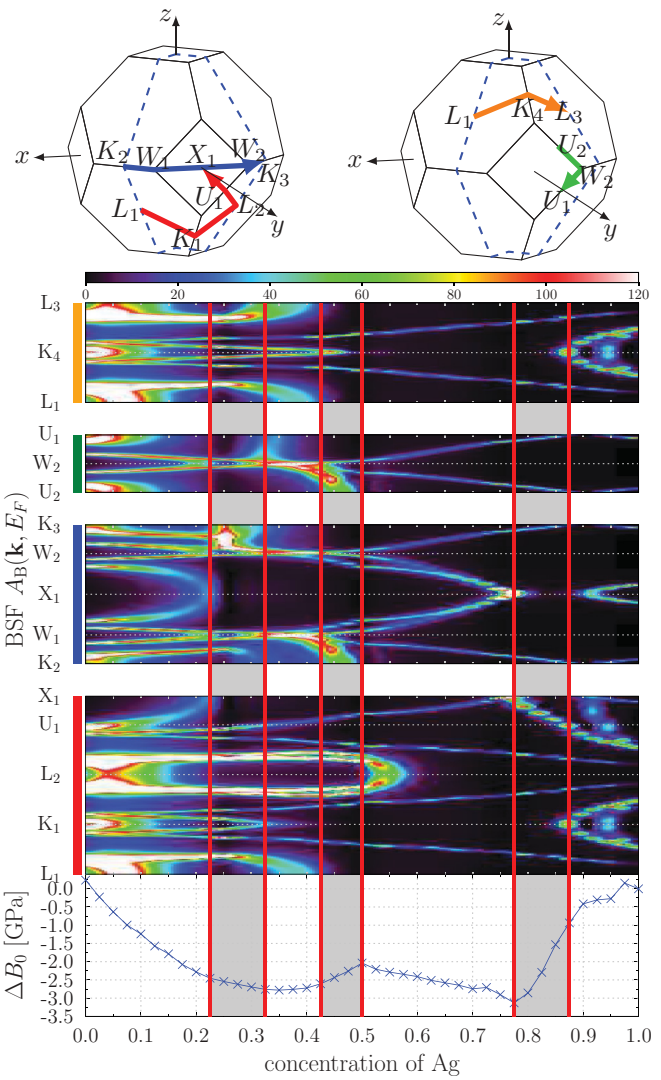

FIG. 7. (Color) Reciprocal space paths (top, color-coded), Bloch spectral function at the Fermi level (middle, in arbitrary units) and nonlinear component of the bulk modulus for the setup of Fig. 1, considered in a LRO regime (see text). The connecting red lines are applied in the same manner as in Fig. 4.

with each others, and the corresponding ΔB_0^{ES} curve shows more pronounced variations that relate more clearly with the BSF results. We can observe, in particular, two ETT's, at $\mathbf{X}_1$ for $c \approx 0.775$ and $\mathbf{K}_1$ or $\mathbf{K}_4$ for $c \simeq 0.875$. For ΔB_0^{ES}, these translate into sharp kinks, and rather homogeneous slopes in the featureless regions in between ($c \in [0.5, 0.775]$ and $c \in [0.775, 0.875]$).

B. Short-range order

The above study may be complemented by considering a distinct regime of partial order for the same $\mathrm{Ag}_c\mathrm{Pd}_{1-c}$ alloy. Previous results in Sec. IV A pertained to the assumption of some periodically repeating sublattices being kept fixed at $c_s = 1$ or 0, and fully uncorrelated occupation of the remaining ones within the single-site, multisublattice CPA[31] (MS-CPA).

We now examine the case of a SRO regime, where no sublattice is kept at integer occupancy. Multisite Ag ↔ Pd

replacements are assumed, with a different substitutions' statistics to reflect the higher stability of the LRO $L1_1^+$, $L1_1$, and $L1_2$ structures initially reported in the literature.

Our treatment is based on the multisublattice nonlocal extension of the original CPA theory. The goal of this development is the self-consistent construction of a richer effective medium description for the partially disordered system, where the condition of on-average no extra scattering from any portion of the bulk is generalized to multisite substitutions involving more than an atom at the time.[9,10]

The corresponding scattering path operator that replaces Eq. (2) reads, in particular:

$$\underline{\overline{\tau}}^{I;J}_{s;s'}(\epsilon) = \frac{1}{\Omega}\sum_{n=1}^{N_c}\left\{\int_{\Omega_{\mathbf{K}_n}} d^3k[\underline{\overline{t}}^{ss'}(\mathbf{K}_n,\epsilon) - \underline{G}'^{0ss'}(\mathbf{k},\epsilon)]^{-1}\right\}_{I,s;J,s'} \times e^{+i\mathbf{K}_n\cdot(\mathbf{R}_I-\mathbf{R}_J)}, \quad (5)$$

where $\{\mathbf{K}_n\}$ denotes a set of $I,J = 1,\ldots,N_c$ "cluster momenta"[8] in a coarse grained treatment of reciprocal space.[32] The original Brillouin zone Ω is now partitioned into subregions $\Omega_{\boldsymbol{K}_n}$ of alike effective medium properties, while explicit dependence on the direct space sublattice indexes $s,s' = 1,\ldots,N_{\rm sub}$ and a matching phase modification of the structure constants allows to generalize the original nonlocal treatment to cases of complex unit cells in arbitrary geometries.

The established CPA procedure for the self-consistent determination of the effective medium is then followed straightforwardly. In particular,different assumptions concerning the degree of SRO to be modeled enter the framework in terms of a multisite probability distribution $P(\gamma)$ for combined elements substitutions,or replacements of whole complexes of $N_{\rm tot} = N_c \times N_{\rm sub}$ atoms:

$$\underline{\overline{\tau}}(\epsilon) = \sum_{\gamma}^{N_{\rm tot}} P(\gamma)\underline{\overline{\tau}}_{\gamma}(\epsilon). \quad (6)$$

In this case study, we adapt $N_c = 1$, and γ labels each of the possible $N_{\rm tot} = 2^{N_{\rm sub}} = 256$ arrangements of 8 Ag or Pd atoms within the extended geometry of Fig. 1/Table I. We include therefore beyond-single-site effects up to the length scale set by our $N_{\rm sub} = 8$ supercell, even if considered as a single cluster in the spirit of the original NL-CPA.[33]

The framework allows to recover LRO results when only one, periodically repeating configuration occurs with probability one. Single-site results are reproduced when a fully uncorrelated probability distribution $P(\gamma) = \prod_{I,s}^{N_c;N_{\rm sub}} c_{I,s}$ over more possibilities is instead adopted. Intermediate scenarios and different forms of SRO can also be set up[8,9] by properly tuning such statistics.

For this particular case study, we adopt the simplified perspective of considering how the gradual collapse of the $L1_1^+$, $L1_1$, or $L1_2$ reference LRO structures above into a fully disordered scenario may reflect on variations in the BSF.

Such scenarios can be described by restricting the probability distribution of multisite replacements only to the set of possibilities listed in Table III. As opposed to previous section, here no sublattice is kept fixed at integer $c_s = 1$ or 0 occupancy, but all are allowed to host either Ag or Pd atoms, with a probability that gives back the desired total concentration while favoring structures related to the reference LRO templates.

TABLE III. Configurations for the inclusion of SRO in the [0.25,0.5] and [0.5,0.75] regimes. The probability is taken from Table IV.

Config.	$c_s, s = 1,\ldots,N_{\rm sub}$	structure	$P(\gamma)$
γ_{1a}	1. 0. 0. 0. 0. 1. 0. 0.	$L1^+$ in	$[1 - p_{1\leftrightarrow 2}(c)]/4$
γ_{1b}	0. 0. 0. 0. 1. 1. 0. 0.	its 4 local	$[1 - p_{1\leftrightarrow 2}(c)]/4$
γ_{1c}	1. 1. 0. 0. 0. 0. 0. 0.	permutations	$[1 - p_{1\leftrightarrow 2}(c)]/4$
γ_{1d}	0. 1. 0. 0. 1. 0. 0. 0.	...	$[1 - p_{1\leftrightarrow 2}(c)]/4$
γ_{2a}	1. 0. 0. 0. 0. 1. 1. 1.	$L1_1$ in	$p_{1\leftrightarrow 2}(c)/8$
γ_{2b}	0. 1. 0. 0. 1. 0. 1. 1.	its 8 local	$p_{1\leftrightarrow 2}(c)/8$
γ_{2c}	0. 0. 1. 0. 1. 1. 0. 1.	permutations	$p_{1\leftrightarrow 2}(c)/8$
γ_{2d}	0. 0. 0. 1. 1. 1. 1. 0.	...	$p_{1\leftrightarrow 2}(c)/8$
γ_{2e}	1. 1. 1. 0. 0. 0. 0. 1.	...	$p_{1\leftrightarrow 2}(c)/8$
γ_{2f}	1. 1. 0. 1. 0. 0. 1. 0.	...	$p_{1\leftrightarrow 2}(c)/8$
γ_{2g}	1. 0. 1. 1. 0. 1. 0. 0.	...	$p_{1\leftrightarrow 2}(c)/8$
γ_{2h}	0. 1. 1. 1. 1. 0. 0. 0.	...	$p_{1\leftrightarrow 2}(c)/8$
γ_{3a}	0. 1. 1. 1. 0. 1. 1. 1.	$L1_2$ in	$[1 - p_{2\leftrightarrow 3}(c)]/4$
γ_{3b}	1. 0. 1. 1. 1. 0. 1. 1.	its four local	$[1 - p_{2\leftrightarrow 3}(c)]/4$
γ_{3c}	1. 1. 0. 1. 1. 1. 0. 1.	permutations	$[1 - p_{2\leftrightarrow 3}(c)]/4$
γ_{3d}	1. 1. 1. 0. 1. 1. 1. 0.	...	$(1 - p_{2\leftrightarrow 3}(c))/4$

As a preliminary validation step for our MS-NL-CPA investigation, we reexamine the concentration interval $c \in [0.25,0.75]$ of Fig. 7, assuming in particular for $c \in [0.25,0.5]$ the SRO restriction to configurations γ_1 and γ_2, and for $c \in [0.5,0.75]$ the configurations γ_2 and γ_3, with probabilities given in Table IV.

In this arrangement, similarly to the previous LRO calculation setup of Sec. IV, a set of six sites $\mathbf{a}_1,\ldots\mathbf{a}_6$ for $\gamma_1 \leftrightarrow \gamma_2$, and 4 fixed sites $\mathbf{a}_5,\ldots\mathbf{a}_8$ for $\gamma_2 \leftrightarrow \gamma_3$, is kept periodically repeated. Agreement in the corresponding effective medium observables is then indeed recovered, both at the level of the resulting bulk modulus, and for the Bloch spectral function.

We then proceed to the study of proper SRO regimes, where no fixed occupancy is set up on any periodically repeating sublattice. This corresponds to relaxing the previous constraints on allowed multisite cavity arrangements. The same tentative structures can be thus locally realised in different orientations within the bulk.

According to this model, for the concentration range $c \in [0.25,0.75]$ the first γ_1 configuration associated with a $L1_1^+$

TABLE IV. Configurations γ_i with $i = 1,2,3$ used for the Bloch spectral function of Fig. 7, for the concentration range $c \in [0.25,0.5]$ and $c \in [0.5,0.75]$. For the first interval $\gamma_1 \leftrightarrow \gamma_2$, the probability $p_{1\leftrightarrow 2}$ is a linear function of the concentration $p_{1\leftrightarrow 2}(c) = 4c - 1$, with $p_{1\leftrightarrow 2}(0.25) = 0$ and $p_{1\leftrightarrow 2}(0.5) = 1$. For the second interval $\gamma_2 \leftrightarrow \gamma_3$, the slope of the concentration dependent probability function is negative, $p_{2\leftrightarrow 3}(c) = 3 - 4c$. Thereby for 0.5 the probabilities are the same for both functions $p_{2\leftrightarrow 3}(0.5) = 1$ and $p_{2\leftrightarrow 3}(0.75) = 0$.

	$c_s, s = 1,\ldots,N_{\rm sub}$	c	structure	$P(\gamma)$
γ_1	1. 0. 0. 0. 0. 1. 0. 0.	0.25	$L1_1^+$	$1 - p_{1\leftrightarrow 2}(c)$
γ_2	1. 0. 0. 0. 0. 1. 1. 1.	0.5	$L1_1$	$p_{1\leftrightarrow 2}(c)$
γ_3	0. 1. 1. 1. 0. 1. 1. 1.	0.75	$L1_2$	$1 - p_{2\leftrightarrow 3}(c)$

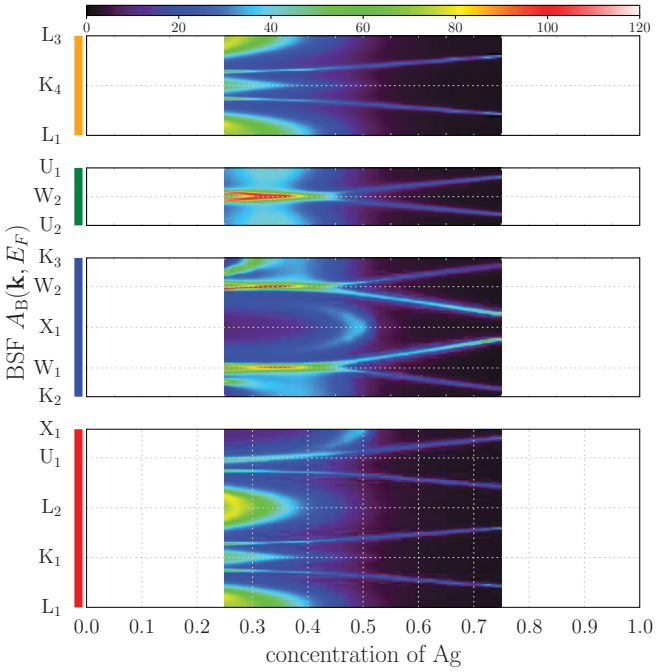

FIG. 8. (Color) SRO $\neq 0$: Bloch spectral function at the Fermi energy along the same paths as in Fig. 7, joining the two concentration ranges $c \in [0.25,0.5]$ and $c \in [0.5,0.75]$ of Ag_cPd_{1-c} in a single representation of the concentration range of interest in this part of the study. Short-range ordering is defined by a restriction to the configurations listed in Table III.

arrangement may branch into four locally equivalent orientations $\gamma_{1a}, \ldots, \gamma_{1d}$, each occurring with same probability. The same approach is also applied to the second case of the γ_2 configuration for the $L1_1$ structure and the γ_3 configuration for the $L1_2$ structure, to give the full listing reported in Table III.

With this different set up our evaluation of the BSF as a function of total concentration undergoes the changes depicted in Fig. 8. As long-range ordering begins to collapse, we observe a degree of softening in all the Fermi surface features when compared with the supercell approach results of Fig. 7. This occurs in particular for the Pd-rich portion of the phase diagram. The previously nonequivalent high symmetry points $\mathbf{L}_1$, $\mathbf{K}_1$, and $\mathbf{W}_1$ begin to recover the original degeneracy across the respective $\mathbf{K}_2$, $\mathbf{K}_3$ anisotropic instances. While for $c > 0.5$ concentrations, a similar sp band structure for the two elements leads to only minor differences in features at the Fermi energy in all the different single-site CPA, LRO and SRO regimes (see Figs. 4, 7, and 8), the d-bands-dominated section begins to show traces of the same outlook obtained in the fully uncorrelated scenario.

At $\mathbf{X}_1$ for instance, the merging of two BSF branches around $c \approx 0.45$ hints towards the corresponding topology already probed in the evaluation of Fig. 4. Similarly, in the neighborhood of $\mathbf{L}_1$ our SRO setup shows how the corresponding single-site feature begins to develop from the LRO starting point of Fig. 7. In general, an alike Fermi surface shape is retained in both treatments, this time with a more spread out appearance. For example, a bifurcation in A_B^{ES} , originally observed around $c = 0.4$ at $\mathbf{L}_1$, remains unresolved

TABLE V. Bulk modulus at the Ag:Pd ratios of the predicted LRO structures,[6] computed in the three ordering regimes considering in this study: the extended unit cell of Fig. 1, the particular SRO regime given in Table III, and the fully uncorrelated scenario described by the single-site CPA. Elastic properties appear in substantial agreement across all investigation, with an outcome of SRO calculations fitting in between the more and less disordered setups.

B_0 (GPa)	$c = 0.25$	$c = 0.5$	$c = 0.75$
Extended setup	193.20	172.14	149.70
Short-range order	192.68	171.35	150.46
single site	192.90	171.12	150.65

in the SRO setup all the way down to $c = 0.25$. The sharp structure at $\mathbf{W}_1$ also undergoes similar modifications.

From the point of view of bulk modulus calculations, a comparison of B_0^{SRO} results for $c = 0.25$, 0.5, and 0.75 with both supercell and the single-site CPA setup is reported in Table V. Our SRO setup leads to predicting elastic properties close to the single-site CPA model for the alloy. The averaging over all main orientations of a reference structure (e.g. four orientations for $L1_1^+$, see Table III) with the MS-NL-CPA seems to lead to a structural situation which is already approaching the fully random distribution in the CPA. The same trend can also be observed for the equilibrium lattice constant.

V. CONCLUSIONS

This work has demonstrated the practical possibility of tracking a suggested connection between deviations from Vergard's rule, or elastic anomalies, and topology changes in the Fermi surfaces or Lifshitz transitions at specific constituents concentrations for the prototype Ag_cPd_{1-c} solid solution. Results from fully uncorrelated, single-site CPA calculations performed in the KKR and EMTO methods have been complemented with an investigation of a variety of LRO and SRO regimes, based on input from independent systematic search for most stable crystalline structures at different concentrations.

Results from an extended unit cell construction, here adopted to account for such findings, could be interpreted in terms of varying structural anisotropy as the system is biased towards any of the predicted $L1_1^+$, $L1_1$, and $L1_2$ fully ordered phases. In particular, recent technical developments on the systematic inclusion of beyond single-site effects in the CPA have led to a more complete analysis of intermediate scenarios. BSF and bulk modulus results appear to fit in between previous fully disordered scenarios, and the new outlook of a partially ordered phase diagram.

Besides elastic properties, the presented technique can also be used to investigate other physical properties within the whole regime of ordering, from total disorder via SRO to LRO, and within the whole concentration range of alloys. Beside ordinary alloys, a similar outlook may be found useful in investigating properties of artificial structures, e.g., multilayers, where the effects are expected to be even more pronounced compared to the present case.

ACKNOWLEDGMENTS

We gratefully acknowledge financial support by the Deutscher Akademischer Austauschdienst (DAAD) and the Academy of Finland (Grant No.134270). We wish to express our gratitude for inspiring discussion and insightful suggestions to Sergei Ostanin (MPI-Halle) and Julie B. Staunton (University of Warwick). L.V. acknowledges the support from the Swedish Research Council, and the Hungarian Scientific Research Fund (research project OTKA 84078).

*hoffmann@mpi-halle.mpg.de

[1] L. Vegard, Z. Phys. A **5**, 17 (1921).

[2] E. Bruno, B. Ginatempo, E. S. Guiliano, A. V. Ruban, and Y. K. Vekilov, Phys. Rep. **249**, 353 (1994).

[3] E. Bruno, B. Ginatempo, and E. S. Giuliano, Phys. Rev. B **52**, 14544 (1995).

[4] E. Bruno, B. Ginatempo, and E. S. Giuliano, Phys. Rev. B **52**, 14557 (1995).

[5] E. K. Delczeg-Czirjak, L. Delczeg, M. Ropo, K. Kokko, M. P. J. Punkkinen, B. Johansson, and L. Vitos, Phys. Rev. B **79**, 085107 (2009).

[6] S. Müller and A. Zunger, Phys. Rev. Lett. **87**, 165502 (2001).

[7] A. V. Ruban, S. I. Simak, P. A. Korzhavyi, and B. Johansson, Phys. Rev. B **75**, 054113 (2007).

[8] D. A. Rowlands, A. Ernst, B. L. Györffy, and J. B. Staunton, Phys. Rev. B **73**, 165122 (2006).

[9] A. Marmodoro, Ph.D. thesis, University of Warwick, 2011.

[10] A. Marmodoro, A. Ernst, and J. B. Staunton, arXiv:1206.5981v1.

[11] B. R. Coles, J. Inst. Met. **84**, 346 (1955).

[12] *Landolt-Boernstein Group III: Electrical Properties Low Frequency Properties of Dielectric Crystals Second and Higher Order Elastic Constants* (Springer-Verlag, Berlin, 1992).

[13] J. Hafner, *From Hamiltonians to Phase Diagrams: the Electronic and Statistical-Mechanical Theory of sp-bonded Metals and Alloys*, Springer Series in Solid-State Sciences (Springer-Verlag, Berlin, 1987).

[14] H. Ebert, D. Ködderitzsch, and J. Minár, Rep. Prog. Phys. **74**, 096501 (2011).

[15] L. Vitos, H. Skriver, and B. Johansson, Comput. Mater. Sci. **18**, 24 (2000).

[16] L. Vitos, Phys. Rev. B **64**, 014107 (2001).

[17] L. Vitos, P. Korzhavyi, and B. Johansson, Nat. Mater. **2**, 25 (2003).

[18] L. Vitos, *Computational Quantum Mechanics for Materials Engineering* (Springer-Verlag, London, 2007).

[19] J. Kollár, L. Vitos, and H. Skriver, Lect. Notes Phys. **535**, 85 (2000).

[20] B. L. Györffy, Phys. Rev. B **5**, 2382 (1972).

[21] J. P. Perdew, A. Ruzsinszky, G. I. Csonka, O. A. Vydrov, G. E. Scuseria, L. A. Constantin, X. Zhou, and K. Burke, Phys. Rev. Lett. **100**, 136406 (2008).

[22] J. P. Perdew and Y. Wang, Phys. Rev. B **45**, 13244 (1992).

[23] F. Birch, Phys. Rev. **71**, 809 (1947).

[24] A. R. Oganov and P. I. Dorogokupets, Phys. Rev. B **67**, 224110 (2003).

[25] V. L. Moruzzi, J. F. Janak, and K. Schwarz, Phys. Rev. B **37**, 790 (1988).

[26] F. D. Murnaghan, PNAS **30**, 244 (1944).

[27] C. L. Fu and K. M. Ho, Phys. Rev. B **28**, 5480 (1983).

[28] The Ag_cPd_{1-c} compound is a heterovalent system. Silver contributes one free electron from its unfilled s shell ($Z_{Ag} = 1$), while for Pd it is $Z_{Pd} = 2$. The electron radius for Ag is taken from Ref. 13 with $R_S^{Ag} = 3.02$ a.u. whereas the radius for Pd is fitted to the single-site ($R_S^{Pd} = 2.96$ a.u.) or experimental ($R_S^{Pd} = 2.93$ a.u.) values. The latter radii do not agree with the references radius of Pd $R_S^{Pd} = 2.6$ a.u., which shows the insufficiency of this simple model to describe the complete physical system.

[29] V. L. Moruzzi and C. B. Sommers, *Calculated Electronic Properties of Ordered Alloys : a Handbook* (World Scientific, Singapore, 1995), p. 421.

[30] E.-K. Delczeg-Czirjak, E. Nurmi, K. Kokko, and L. Vitos, Phys. Rev. B **84**, 094205 (2011).

[31] A. J. Pindor, W. M. Temmerman, and B. L. Györffy, J. Phys. F **13**, 1627 (1983).

[32] M. Jarrell and H. R. Krishnamurthy, Phys. Rev. B **63**, 125102 (2001).

[33] D. A. Rowlands, J. B. Staunton, and B. L. Györffy, Phys. Rev. B **67**, 115109 (2003).